JUSTC

Article

http://justc.ustc.edu.cn

Received: May 10, 2026; Accepted: May 28, 2026

La and Zr co-doped Ruddlesden–Popper air electrode materials for PCFCs

Xiaoxia Li, Yinghao He, and Ranran Peng ✉

Department of Materials Science and Engineering, University of Science and Technology of China, Hefei, 230026, China

✉Correspondence: Ranran Peng, E-mail: pengrr@ustc.edu.cn

Graphical abstract

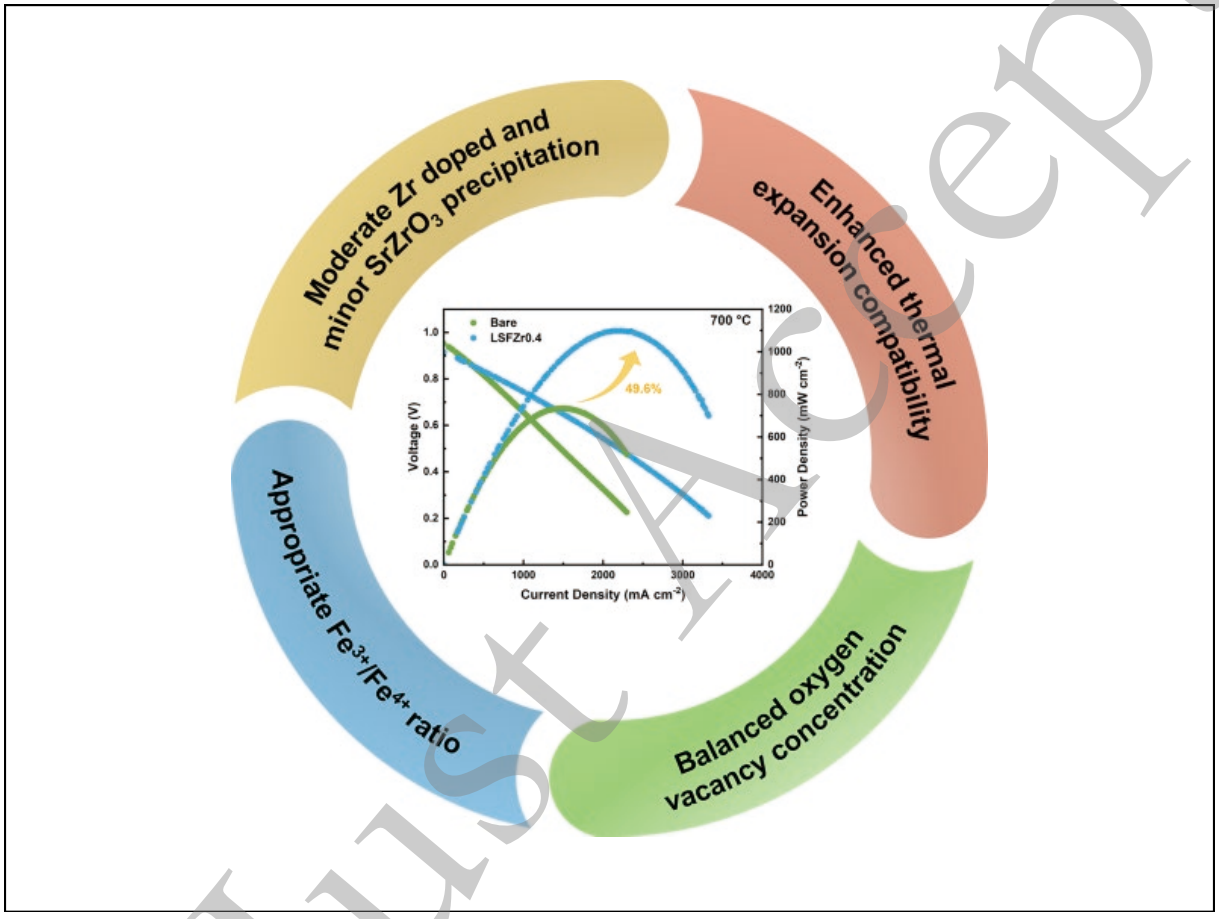

La/Zr codoping modulates material properties and enhances the electrochemical performance of a cobalt-free R-P air electrode for PCFCs.

Public summary

■ La and Zr codoping stabilizes the three-layer Ruddlesden–Popper structure in $Sr_4Fe_3O_{10-\delta}$.

■ Moderate Zr doping (x = 0.4) induces a small amount of the $SrZrO_3$ secondary phase, which improves interfacial contact.

■ LSFZr0.4 has a low polarization resistance of 0.14 Ω cm^2 and a high peak power density of 1098 mW cm^{-2} at 700 °C and outperforms most reported Co-free layered cathodes.

Citation: Li X X, He Y H, Peng R R. La and Zr co-doped Ruddlesden–Popper air electrode materials for PCFCs. *JUSTC*, **2026**, 56(0): . CSTR: 32290.14.JUSTC-2026-0066. DOI: 10.52396/JUSTC-2026-0066

JUSTC

Article

http://justc.ustc.edu.cn

Received: May 10, 2026; Accepted: May 28, 2026

La and Zr co-doped Ruddlesden–Popper air electrode materials for PCFCs

Xiaoxia Li, Yinghao He, and Ranran Peng ✉

Department of Materials Science and Engineering, University of Science and Technology of China, Hefei, 230026, China

✉Correspondence: Ranran Peng, E-mail: pengrr@ustc.edu.cn

Cite This: *JUSTC*, **2026**, 56(X): (9pp) Read Online SI Supporting Information

Abstract: The development of high-performance air electrodes is critical for the practical application of protonic ceramic fuel cells (PCFCs). In this work, a series of Ruddlesden–Popper (RP)-type cathodes with a nominal composition of $La_{0.3}Sr_{3.7}Fe_{3-x}Zr_xO_{10-\delta}$ (x = 0.3, 0.4, 0.5) is synthesized via a modified combustion method. The influence of Zr doping on phase evolution, defect chemistry, and electrochemical activity is systematically investigated. The results reveal that increasing the Zr content gradually reduces the oxygen vacancy concentration, promotes the reduction of Fe^{4+} to Fe^{3+}, and introduces $SrZrO_3$ precipitation (x≥0.4). Nevertheless, among the prepared samples, the $La_{0.3}Sr_{3.7}Fe_{2.6}Zr_{0.4}O_{10-\delta}$ (LSFZr0.4) cathodes exhibit the best electrochemical performance. At 700 °C, the polarization resistance of LSFZr0.4 is 0.14 Ω cm², approximately 26.3%, 22.2%, and 12.5% lower than that of the undoped sample, x = 0.3, and x = 0.5, respectively. The superior electrochemical performance of LSFZr0.4 mainly benefits from its well-matched thermal expansion coefficient, which strengthens the cathode–electrolyte interface and accelerates charge transfer and surface exchange kinetics. In single-cell tests, the LSFZr0.4-based cell delivers a peak power density of 1098.0 mW cm^{-2} at 700 °C, which is more than 200 mW cm^{-2} greater than those of the x = 0.3 and x = 0.5 cathodes. This work provides a promising air electrode for PCFCs and demonstrates that moderate Zr doping is an effective strategy for optimizing the performance of RP-type cathodes.

Keywords: Ruddlesden–Popper layered cathodes; Protonic ceramic fuel cells; La, Zr codoped; phase separation

CLC number: TM91 **Document code:** A

1 Introduction

The escalating global energy crisis and the urgent need to reduce carbon emissions have driven intensive research into efficient and clean energy conversion technologies. Compared with conventional oxygen-ion conducting solid oxide fuel cells, PCFCs have emerged as promising candidates for intermediate-temperature operation (400–700 °C)[1], offering high theoretical efficiency, low activation overpotentials, and excellent fuel flexibility. However, the practical application of PCFCs is largely hindered by sluggish oxygen reduction reaction (ORR) kinetics at the air electrode, as well as inadequate chemical and thermal compatibility between the electrode and the proton-conducting electrolyte[2,3].

The air electrode is the site of the ORR. An ideal material must possess high electronic and ionic conductivity, good catalytic activity, and a thermal expansion coefficient matching that of the electrolyte[4,5]. Cobalt-based perovskites such as $Ba_{0.5}Sr_{0.5}Co_{0.8}Fe_{0.2}O_{3-\delta}$ (BSCF) offer excellent mixed conductivity and ORR activity, but their high thermal expansion coefficients (>20×10^{-6} K^{-1})[6] cause severe thermal mismatch with typical proton conductors (e.g., $BaZr_{0.1}Ce_{0.7}Y_{0.1}Yb_{0.1}O_{3-\delta}$ and TEC ≈ 11.6×10^{-6} K^{-1})[7], leading to electrode delamination and rapid performance decay during thermal cycling[8]. Moreover, cobalt is scarce and expensive, limiting its large-scale application. Consequently, developing cobalt-free or low-cobalt air electrode materials with both high activity and good thermomechanical stability has become a major research focus[9,10].

Recent efforts have demonstrated that cobalt-free perovskite cathodes can achieve remarkable performance through various modification strategies. For instance, Feng et al.[11] introduced Gd into $BaFe_{0.8}Zr_{0.2}O_{3-\delta}$ and reported that Gd doping simultaneously increased the oxygen vacancy concentration and proton hydration capability, leading to a 1.93-fold improvement in the peak power density. Ye et al.[12] created B-site deficient $Ba_{0.95}La_{0.05}(Fe_{0.8}Zn_{0.2})_{0.95}O_{3-\delta}$ (BLFZ0.95) and concluded that B-site deficiency enhances oxygen vacancy concentration and electronic structure, yielding an area-specific resistance as low as 0.04 Ω cm² at 700 °C. The same group also developed $Ba_{0.95}Pr_{0.05}FeO_{3-\delta}$ (BP5F)[13] by A-site Pr doping and reported that Pr doping stabilized the cubic phase and improved the triple conductivity, resulting in outstanding bifunctional performance in both the SOFC and PCFC modes.

Among the various alternative material systems, Ruddlesden–Popper (RP)-type layered perovskite oxides have attracted extensive research interest because of their unique crystal configuration and excellent mixed conductivity [14,15]. In particular, n = 3 RP-phase strontium ferrate (SFO) is regarded as a highly promising air electrode candidate for PCFCs[16,17] because of its good mixed ionic-electronic conductivity and high intrinsic catalytic activity[18,19]. Studies have shown that

CSTR: 32290.14.JUSTC-2026-0066
DOI: 10.52396/JUSTC-2026-0066
JUSTC, **2026**, 56(X):

SFO-based materials maintain a stable perovskite structure over a wide oxygen partial pressure range and that the presence of mixed Fe^{3+}/Fe^{4+} valence states provides good electronic conductivity [20]. Nevertheless, two major bottlenecks still hinder their practical application: First, the TEC remains relatively high (~23×10^{-6} K^{-1}), resulting in poor thermal matching with the electrolyte[21]; second, Sr surface segregation tends to occur during long-term operation, leading to the degradation of active sites and increased interfacial resistance.

In this work, a series of $La_{0.3}Sr_{3.7}Fe_{3-x}Zr_xO_{10-\delta}$ (x = 0.3, 0.4, 0.5) cathodes with a triple-layer RP structure is synthesized via a tailored combustion method. The effects of the Zr content on the crystal structure, phase composition, thermal stability, electrical conductivity, ORR activity, and single-cell performance are systematically evaluated. An optimal Zr doping level (x = 0.4) induces a minor amount of $SrZrO_3$ secondary phase that acts as an interfacial activator, yielding superior electrochemical output. The solubility limit of Zr at the B site is determined to be between 0.3 and 0.4, and the underlying mechanisms for the balanced ionic transport, charge transfer, and catalytic activity are elucidated. This work not only provides a high-performing air electrode for PCFCs but also reveals a new activation paradigm through controlled secondary phase precipitation.

2 Materials and methods

2.1 Materials and synthesis method

La/Zr-codoped $Sr_4Fe_3O_{10-\delta}$ oxides with a nominal composition of $La_{0.3}Sr_{3.7}Fe_{3-x}Zr_xO_{10-\delta}$ (x = 0.3, 0.4, 0.5) were studied as potential cathode materials for PCFCs. For convenience, these samples were denoted as LSFZrx (x = 0.3, 0.4, and 0.5). The LSFZrx powders were prepared via a combustion method using ethylenediaminetetraacetic acid (EDTA) and citric acid monohydrate (CA) as the complexing agent and reducing agent, respectively. Stoichiometric amounts of La_2O_3 (99.99%), $Zr(NO_3)_4{\cdot}5H_2O$ (99.5%), $Sr(NO_3)_2$ (99.5%), and $Fe(NO_3)_3{\cdot}9H_2O$ (99.5%) were weighed and dissolved sequentially in dilute nitric acid under continuous stirring to form a clear solution. EDTA and CA were then added at a metal ion/EDTA/CA molar ratio of 1:1:1.5. The pH of the solution was adjusted to neutral using an ammonia solution, followed by continuous stirring for at least 2 h to ensure complete complexation. The solution was then transferred to a hot plate and heated until gelation and autoignition occurred, yielding gray-brown ash. The resulting gray-brown precursor was thoroughly ground in an agate mortar until it transformed into a fine, dark-brown powder [14, 22]. An appropriate amount of the ground powder was gently pressed into circular pellets, which were then placed in a corundum crucible and heat-treated in air at 1150 °C for 5 h to obtain the desired crystallization of the cathode powder.

For comparison, $Sr_4Fe_3O_{10-\delta}$ (SFO) was also prepared using the same procedure but calcined at 1150 °C for 5 h. NiO and $BaZr_{0.1}Ce_{0.7}Y_{0.1}Yb_{0.1}O_{3-\delta}$ (BZCYYb) powders were synthesized using the same combustion method. The details of their synthesis procedure can be found elsewhere [23].

Alternatively, BZCYYb1711 powder was synthesized via a conventional solid-state reaction method[24]. The metal precursor powders were accurately weighed according to the stoichiometric ratios, placed in a ball mill jar, and mixed with 250 mL of ethanol and zirconia balls as the grinding media. The mixture was ball-milled in a planetary ball mill at 400 rpm for 24 h. The resulting slurry was then dried and thoroughly ground, followed by heat treatment at 1200 °C for 10 h to obtain the target BZCYYb white powder.

2.2 Fabrication of anode-supported cells and symmetric cells

The composite powder of NiO, BZCYYb, and polymethyl methacrylate (PMMA, pore former) was mixed at a mass ratio of 65:35:10 to serve as the anode powder. After the mixture was ground for 1 h, a polyvinyl alcohol (PVA, binder) solution was added, and the sample was ground for another 1 h until dry anode powder was obtained[25]. Afterward, 0.25 g of the anode powder was placed into a 13 mm-diameter metal mold and uniaxially pressed at approximately 120 MPa for 5 s to form the NiO-BZCYYb anode support. The BZCYYb electrolyte powder prepared by the combustion method was then uniformly spread onto the support, followed by a second pressing at 300 MPa with a holding time of 1 min to obtain the green NiO- BZCYYb|BZCYYb half-cell. The half-cell was sintered at 1350 °C for 5 h to obtain a dense electrolyte film. In the resulting sintered half-cell, the dense electrolyte film was approximately 10 μm thick, and the anode thickness was approximately 480 μm. Then the cathode powder (including 5 wt.% electrolyte powder) was mixed with terpineol at a mass ratio of 1:1.5 and thoroughly ground to prepare a uniform slurry[26]. The slurry was brushed onto the electrolyte surface of the half-cell. After drying, the sample was heated in air at 1000 °C for 2 h to obtain a single cell. The effective coating area of the cathode layer was 0.2376 cm^2.

For symmetric cell fabrication, BZCYYb powder synthesized by the solid-state method was used. BZCYYb was mixed with NiO at a mass ratio of 100:1 as the electrolyte support material, where NiO served as a sintering aid to promote electrolyte densification. Following a similar pressing procedure, 0.25 g of the powder was placed into a 13 mm-diameter mold, pressed at 300 MPa, and then sintered in air at 1500 °C for 5 h to obtain a dense electrolyte pellet. The cathode slurry was subsequently brushed onto both sides of the electrolyte pellet, dried, and calcined at 1000 °C for 2 h to obtain a symmetric cell.

2.3 Fabrication and characterization of rectangular bars

To evaluate the thermal expansion coefficient and electrical conductivity of LSFZrx, dense samples with bar shapes were prepared. An appropriate amount of LSFZrx powder was thoroughly ground until uniform. Following the same grinding and pressing process used for the anode powder, the LSFZrx powder was uniaxially pressed at 300 MPa to obtain a green bar[27]. The bars were sintered at 1380 °C for 5 h in air to get dense.

The electrical conductivity of the dense bar samples was measured using a standard four-probe DC method with a Keithley 2001 multimeter. Four silver wires were attached to the bar as electrodes, in which the two outer probes were used

CSTR: 32290.14.JUSTC-2026-0066
DOI: 10.52396/JUSTC-2026-0066
JUSTC, **2026**, 56(X):

to apply a constant current I, and the two inner probes were used to measure the voltage drop V. Conductive resin (DAD87; Shanghai Research Institute of Synthetic Resins) was applied to improve the contact between the Ag wires and the sample. The conductivity was calculated as $\sigma = (I \times L)/(V \times A)$, where L is the distance between the voltage probes and A is the cross-sectional area of the bar. Measurements were performed at different oxygen partial pressures over a temperature range of 700–300 °C.

2.4 Material characterization

The crystal structure and phase composition of the LSFZr*x* samples were analyzed by X-ray diffraction (XRD) using a Rigaku TTR-III diffractometer with Cu-Kα radiation (λ = 0.1541 nm). Diffraction patterns were recorded over a 2θ range of 20–80° with a step size of 0.02° and a scan speed of 15° min^{-1}. For detailed structural analysis, Rietveld refinement was performed on slow-scan XRD data (3° min^{-1}) using GSAS-II software [28]. Phase identification was carried out by comparing the XRD patterns against the International Center for Diffraction Data (ICDD) PDF-4 reference database using MDI Jade 9.

The microstructures of all the samples were observed using a scanning electron microscope (SEM, HITACHI SU8200). To reveal the atomic morphology and elemental distribution of the LSFZr0.4 sample, high-resolution transmission electron microscopy (HRTEM, Talos F200X) coupled with energy dispersive spectroscopy (EDS) was employed.

X-ray photoelectron spectroscopy (XPS, Thermo ESCALAB 250) was used to investigate the chemical and electronic states of the elements. Thermogravimetric analysis (TGA, DTG-60H) was conducted in an air atmosphere from room temperature to 1000 °C at a heating rate of 10 °C min^{-1} to confirm the weight loss at high temperatures.

2.5 Electrochemical measurement

For symmetric cell characterization, silver paste was applied to the cathode surfaces as a current collector. Then the samples were dried and heated at 600 °C for half an hour. After that, the symmetric cells were placed in an alumina support inside a sealed quartz tube under wet air flow. Electrochemical impedance spectroscopy (EIS) was conducted using an electrochemical workstation (DH7001, Jiangsu Donghua) over a frequency range of 0.01 Hz to 1 MHz with an AC signal amplitude of 20 mV within a temperature range of 550–700 °C.

All single cells were measured in a custom-built fuel cell testing system. During the tests, the anode chamber was supplied with H_2 containing 3 % H_2O at a flow rate of 30 mL min^{-1}, while the cathode chamber received dry air at 10 mL min^{-1}. EIS was measured at temperatures from 550 °C to 700 °C in 50 °C intervals.

3 Results and discussion

3.1 Phase structure and lattice parameter evolution

XRD analysis (Fig. 1a) revealed that undoped $Sr_4Fe_3O_{10-\delta}$ underwent structural decomposition during thermal treatment for synthesis, resulting in the formation of a mixed phase consisting of a two-layered R-P oxide ($Sr_3Fe_2O_{7-\delta}$, PDF#70-1395) and a perovskite, $SrFeO_{3-\delta}$ (PDF#40-0905), as confirmed by the Rietveld refinement results shown in Fig. S1a. In contrast, La and Zr codoping (e.g., LSFZr0.3) successfully stabilized the 3-layer R-P structure (PDF#22-1429)[29]. Notably, for compositions with x≥0.4, an impurity peak corresponding to $SrZrO_3$ (PDF#97-018-7481) appears at ~31°, indicating that the solution limit of Zr in the parent phase lies between *x*=0.3 and 0.4. Beyond this limit, excess Zr reacts with Sr to form a secondary $SrZrO_3$ phase.

The magnified XRD patterns in the 31°–33° range shifted to higher angles as the Zr content increased from *x*=0.3 to 0.5. For example, the main diffraction peak (e.g., the (107) peak) shifted from 31.89° to 31.94° to 32.02°. According to Bragg's law, a shift to a higher angle corresponds to lattice contraction. This lattice contraction can be attributed to two factors: (1) the precipitation of $SrZrO_3$ consumes A-site Sr^{2+}, resulting in a higher relative concentration of smaller La^{3+} in the parent R-P phase; and (2) the enhanced concentration of high-valence La^{3+} (compared with Sr^{2+}) suppresses the oxygen vacancies, further contributing to the lattice contraction.

Rietveld refinement using GSAS II yielded R_{wp} and χ^2 values less than 10%, confirming the high fidelity of the structural models. The refined lattice parameters (Fig. S1, Table S1, see in supporting information) exhibit a systematic decrease with increasing Zr^{4+} content, which is consistent with the observed high-angle peak shifts. Quantitative analysis revealed a secondary phase of cubic $SrZrO_3$ (space group Pm 3 m), whose weight fraction increased from 0% (*x* = 0.3) to 3.2% (*x* = 0.4) and 6.6% (*x* = 0.5). These findings provide quantitative evidence for successful La/Zr incorporation and the resulting phase evolution within the LSFZr*x* system.

The surface morphologies of the LSFZr*x* samples with different doping levels (*x* = 0.3, 0.4, 0.5) are shown in Fig. S2. For the *x* = 0.3 sample, the surface has a smooth morphology without visible precipitates. When the doping concentration increases to *x* = 0.4, a limited number of scattered nanoparticles begin to emerge on the grain surfaces. Upon further increasing the dopant content to *x* = 0.5, a high density of precipitates is observed, indicating a clear concentration-dependent exsolution behavior.

For PCFCs, water vapor is generated at the air electrode, so the electrode material must have good humidity tolerance. To evaluate the structural stability and hydration behavior, LSFZr*x* powders were treated at 600 °C for 10 h in 10 vol% H_2O/air, and the post-treatment XRD patterns are shown in Fig. 1b. All the samples retain a stable RP-tetragonal phase without decomposition. All the powders exhibit lattice expansion (the diffraction peaks shift to lower 2θ), confirming the water uptake and protonation capability. On the basis of the (107) peak position, *x*=0.3 (31.79°, Δ=0.10), *x*=0.4 (31.73°, Δ=0.21), and *x*=0.5 (31.88°, Δ=0.14). The largest expansion of *x*=0.4 indicates that more protons are generated under humid conditions, which is beneficial for proton conductivity.

The chemical compatibility between the electrode and electrolyte is crucial for battery stability and performance. Here, LSFZr*x* and BZCYYb were mixed (1:1 wt.%) and heat-treated at 1000 °C for 2 h to simulate cell fabrication condi-

CSTR: 32290.14.JUSTC-2026-0066
DOI: 10.52396/JUSTC-2026-0066
JUSTC, **2026**, 56(X):

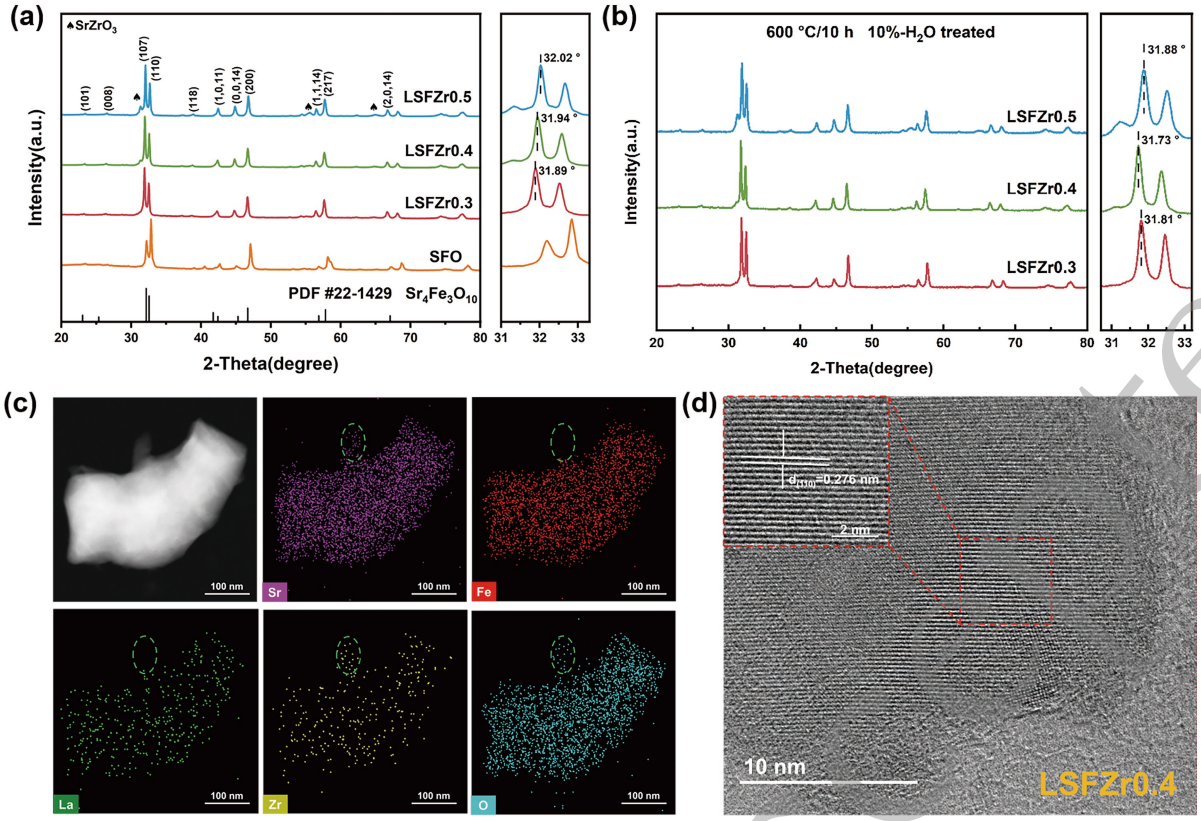

Fig. 1. Phase structure and microstructural characterization of the LSFZrx powders: (a) Room-temperature XRD patterns; (b) XRD patterns of LSFZrx powders after treatment at 600 °C in an atmosphere with 10% water content for 10 h; detailed microstructural analysis of the LSFZr0.4 powder: (c) EDS elemental mappings and (d) HR-TEM micrograph with the indicated lattice d-spacing.

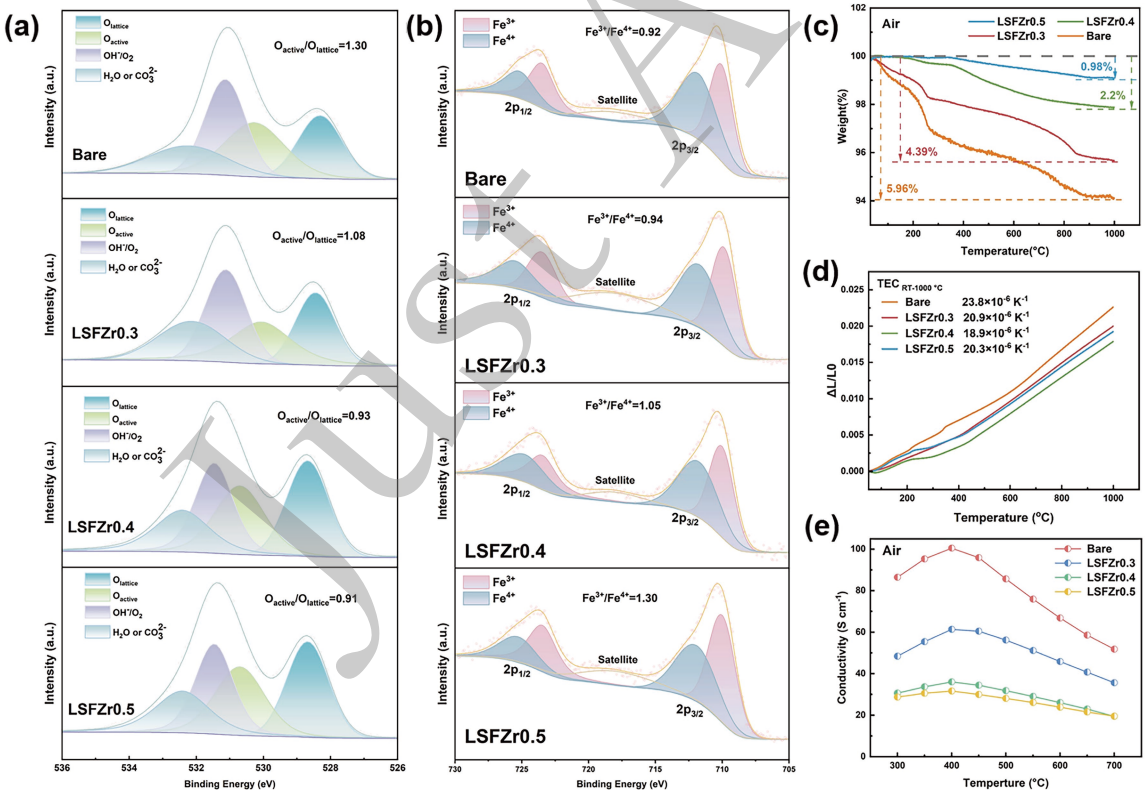

Fig. 2. Physicochemical properties of LSFZr*x* (*x* = 0.3, 0.4, 0.5) powders: (a) O 1 s species and (b) Fe 2p species in the LSFZr*x* powder; (a); (c) TGA curves measured in air; (d) TEC curves from RT-1000 °C; (e) Electrical conductivity in air from 300–700 °C.

CSTR: 32290.14.JUSTC-2026-0066
DOI: 10.52396/JUSTC-2026-0066
JUSTC, **2026**, 56(X):

tions. XRD analysis of the mixture (Fig. S3) revealed only the superimposed patterns of the individual LSFZrx and BZCYYb phases, with no additional diffraction peaks. This finding indicates that no significant chemical reaction or interdiffusion occurs under the tested conditions, confirming good chemical compatibility. These findings support reliable single-cell fabrication and long-term operation.

The elemental distribution of the LSFZr0.4 powder is shown in Fig. 1c. The mapping results indicate that La, Sr, Fe, and Zr are generally homogeneously distributed, although a few Sr- and Zr-rich agglomerates are also observed, which is consistent with the $SrZrO_3$ diffraction peaks detected by XRD. To further confirm the microstructure, the sample was characterized by HR-TEM. As shown in Fig. 1d, the measured lattice fringe spacing is 0.276 nm, which is in agreement with the calculated spacing of the (110) plane. These results are in good agreement with the interplanar spacing derived from the XRD structural analysis, further validating the accuracy of the crystal structure refinement.

3.2 Surface and physicochemical properties

X-ray photoelectron spectroscopy (XPS) was used to analyze the effects of La and Zr co-doping on the chemical states of Fe and O in LSFZr*x* (Fig. 2a–b). In the O 1 s spectra, the peak at ~528.5 eV (lattice oxygen, O^{2-}) intensifies with increasing Zr content. The peak fitting of O 1 s identifies four components: lattice oxygen (O^{2-}, ~528.6 eV), reactive oxygen (O^{-}/O_2^{2-}, ~530.2 eV), hydroxyl/adsorbed oxygen (OH^{-}/O_2, ~531.2 eV), and adsorbed water/carbonate (~532.3 eV)[30]. As Zr doping increases, the relative area of the lattice oxygen peak increases significantly, indicating suppressed loss of lattice oxygen and reduced oxygen vacancy concentration, which enhances structural stability. The ratio of reactive oxygen to lattice oxygen decreases with increasing Zr content from 1.30 (undoped) to 1.08 (LSFZr0.3), 0.93 (LSFZr0.4), and 0.91 (LSFZr0.5), confirming that lattice oxygen is more firmly fixed.

In the Fe 2p spectra ($2p_{3/2}$ and $2p_{1/2}$), Fe^{3+} peaks appear at 710.1 and 723.3 eV, and Fe^{4+} peaks appear at higher binding energies (712.1 and 725.0 eV)[31]. Quantitative analysis reveals that the Fe^{3+}/Fe^{4+} ratio increases progressively with increasing Zr doping: from 0.92 (undoped) to 0.94 (LSFZr0.3), 1.05 (LSFZr0.4), and 1.30 (LSFZr0.5). This finding indicates that a higher Zr content promotes the reduction of Fe^{4+} to Fe^{3+}.

The underlying charge compensation mechanism is as follows. With increasing Zr doping, secondary phase $SrZrO_3$ precipitates (negligible at x=0.3, minor at x=0.4, and significant at x=0.5). The formation of $SrZrO_3$ selectively consumes Sr^{2+} and Zr^{4+} from the RP matrix, thereby increasing the relative proportion of La^{3+} in the A-sites of the remaining perovskite layers. Since La^{3+} has a higher valence than Sr^{2+}, its substitution introduces an additional positive charge into the lattice. To compensate for this excess positive charge, the system employs two possible mechanisms: (1) reducing the oxygen vacancy concentration (which has an effective positive charge) or (2) reducing high-valence cations ($Fe^{4+} \rightarrow Fe^{3+}$, which consumes electrons). The O 1 s spectra reveal an increased fraction of lattice oxygen, indicating a decrease in the oxygen vacancy concentration, which is consistent with mechanism (1). Moreover, the increasing Fe^{3+}/Fe^{4+} ratio confirms that mechanism (2) also occurs. Both pathways work synergistically to maintain charge neutrality.

To investigate the effect of Zr doping on thermal behavior, LSFZrx powders were analyzed by TG in air (Fig. 2c). Undoped SFO and LSFZr0.3 show total weight losses of 5.68 wt.% and 4.39 wt.%, respectively, with three stages: RT-100 °C (adsorbed water), 200-300 °C (lattice water), and 700-900 °C (lattice oxygen release, O-vacancy formation). High-doped samples LSFZr0.4 and LSFZr0.5 also exhibit three stages but with shifted temperatures: negligible RT-200 °C loss, a small loss at 200–400 °C, and a significant loss above 400 °C, stabilizing near 900 °C; total losses are 2.2 wt.% and 0.98 wt.%, respectively. The greatest loss in SFO is due to fewer R-P layers (enhanced water absorption) and weaker metal-oxygen bonds. Increasing the Zr content reduces total loss, indicating that La/Zr co-doping suppresses O-vacancy formation and lattice oxygen release. High Zr doping also decreases the O-vacancy concentration and inhibits hydration (Eq. 1), reducing the number of proton defects (less loss at 200–400 °C). These results are consistent with the XPS data (a higher Fe^{3+}/Fe^{4+} ratio and lower reactive/lattice oxygen content), confirming the presence of fewer oxygen vacancies and enhanced thermal stability.

$$O_O^{\times} + V_O^{\cdot\cdot} + H_2O \rightarrow 2OH_O^{\cdot} \quad (1)$$

To evaluate the thermal compatibility of the LSFZr*x* cathodes, thermal expansion coefficients (TECs) were measured from room temperature to 1000 °C (Fig. 2d). Undoped SFO has the highest TEC of 23.8×10^{-6} K^{-1}, whereas LSFZr0.4 has the lowest at 18.9×10^{-6} K^{-1}. LSFZr0.3 and LSFZr0.5 exhibit similar intermediate values (20.9×10^{-6} K^{-1} and 20.3×10^{-6} K^{-1}, respectively). The high TEC of SFO results from weak lattice bonding, which causes intense lattice vibrations and chemical expansion from oxygen loss at high temperatures. Introducing La^{3+} and Zr^{4+} suppresses both physical and chemical expansion, lowering the TEC. Although LSFZr0.5 loses even less lattice oxygen, excess $SrZrO_3$ precipitation may introduce microcracks or interfacial stress, complicating its thermal expansion. Therefore, LSFZr0.4 offers the best thermal expansion behavior for good matching with common electrolytes and long-term stability.

The electrical conductivity of the LSFZr*x* samples was measured by the four-probe method (Fig. 2e). In the range of 300–700 °C, the conductivity of all the samples first increases but then decreases, with a peak at approximately 400 °C. The decrease at higher temperatures is attributed to the release of lattice oxygen (Eq. (2)), as excess oxygen vacancies serve as electron scattering centers or random traps, lowering carrier mobility and thus decreasing electrical conductivity[32]. For the doped samples, the conductivity generally decreases with increasing Zr^{4+} content. This is because appropriate Zr doping suppresses the formation of oxygen vacancies and electron holes, thereby reducing the overall conductivity. These results are in good agreement with the results of the thermogravimetric and XPS analyses, collectively revealing the regulation of defect chemistry and transport properties by Zr doping.

CSTR: 32290.14.JUSTC-2026-0066
DOI: 10.52396/JUSTC-2026-0066
JUSTC, **2026**, 56(X):

$$O_O^{\times} + 2h^{\cdot} \rightarrow V_O^{\cdot\cdot} + 1/2O_2 \quad (2)$$

3.3 Electrochemical performance of symmetric cells

To evaluate the oxygen reduction reaction (ORR) activity of the LSFZrx air electrode, electrochemical impedance spectroscopy (EIS) was performed on symmetric cells with the LSFZrx|BZCYYb|LSFZrx configuration in the temperature range of 550–700 °C under humid air (3 vol% H_2O). Moreover, the EIS spectra measured in dry air are shown in Fig. S4. Although the total polarization resistances in dry and humid air are similar, the spectral features differ notably; i.e., compared with those in the humid-air case, the medium-frequency arc in dry air becomes larger, whereas the low-frequency arc decreases. These results suggest that under humid conditions, the adsorption/dissociation kinetics are retarded, whereas the charge transfer kinetics are accelerated. Such behavior can be attributed to a shift in the dominant charge carrier in the electrolyte from oxygen ions to protons, which consequently alters the reaction mechanism at the cathode. The ohmic resistance (R_o) was subtracted from all the EIS spectra for direct comparison of the polarization resistances, as shown in Fig. 3(a–d). The polarization resistances exhibit a non-monotonic trend with Zr doping. For example, at 600 °C (Fig. 3e), the order is LSFZr0.4 (e.g., 1.08 Ω cm^2) < LSFZr0.5 (e.g., 1.22 Ω cm^2) < LSFZr0.3 (e.g., 1.45 Ω cm^2) < Bare (e.g., 1.51 Ω cm^2). This behavior is likely related to the hydration capability of the LSFZr*x* materials. The strongest hydration of LSFZr0.4 facilitates proton uptake and transport, thereby reducing the charge-transfer resistance and enhancing the ORR activity. However, when $x = 0.5$, it exhibits moderate hydration, but its excess $SrZrO_3$ secondary phase may partially block active sites or proton pathways, resulting in a slightly higher resistance. In contrast, LSFZr0.3 has the weakest hydration, leading to the highest polarization resistance.

For the symmetric cells measured at 700 °C, the EIS spectra were fitted using the equivalent circuit model R-(RHF//CPEHF-)-(RIF//CPEIF)-(RLF//CPE LF), where R and CPE denote a resistor and a constant phase element, respectively. The fitting resolves the spectra into three arcs corresponding to the high-, intermediate-, and low-frequency regions, which are attributed to oxygen adsorption/dissociation, charge transfer, and ionic diffusion processes, respectively. As shown in Fig. 3f, LSFZr0.4 exhibits the lowest charge transfer and oxygen adsorption/dissociation resistance among all the samples, demonstrating the best electrode kinetics at 700 °C. Although its ionic transport resistance is slightly higher than that of LSFZr0.3, the overall electrode performance is optimal for $x = 0.4$.

3.4 Electrochemical performance of single cells

To evaluate the La/Zr co-doped SFO for PCFCs, anode-supported single cells (NiO-BZCYYb|BZCYYb|LSFZr*x*) were fabricated. The I-V-P curves (Fig. 4a, b and Fig. S5) indicate that the peak power density (PPD) of each cell increases with temperature, due to accelerated electrode kinetics and reduced polarization resistance. A comparison of the performance at 700 °C is shown in Fig. S6: the PPD follows LSFZr0.4 (1098.0 mW cm^{-2}) > LSFZr0.5 (899.3 mW cm^{-2}) > LSFZr0.3 (871.2 mW cm^{-2}) > SFO (733.9 mW cm^{-2}). The superior performance of LSFZr0.4 confirms that an appropriate Zr doping level (x=0.4) optimizes the electrochemical properties. Compared with previously reported cobalt-free R-P phase cathodes, the cell using the LSFZr0.4 cathode exhibits excellent performance at the investigated operating temperature, as shown in Fig. 4(e).

To investigate the effect of Zr doping on the electrochemical activity of LSFZr*x* cathodes, electrochemical impedance spectroscopy was performed on single cells under open-circuit voltages at 550–700 °C. The Nyquist plots of the different samples are shown in Fig. S7. The polarization resistance follows the order of LSFZr0.4 < LSFZr0.5 < LSFZr0.3 <

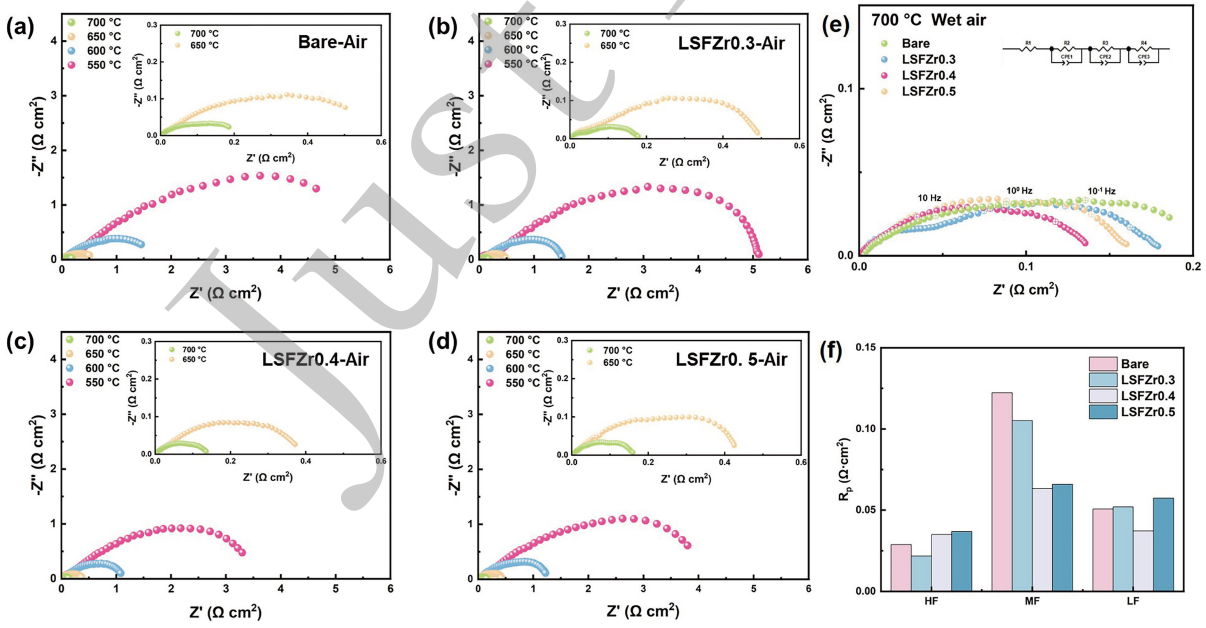

Fig. 3. EIS Nyquist plots of SFO and LSFZr*x* (x = 0.3, 0.4, 0.5) symmetric cells measured in humid air (3% H_2O) at 550–700 °C: (a) Bare SFO, (b) x=0.3, (c) x=0.4, (d) x=0.5. (e) Comparison of EIS spectra at 700 °C. (f) Fitted polarization resistances of three frequency ranges at 700 °C.

CSTR: 32290.14.JUSTC-2026-0066
DOI: 10.52396/JUSTC-2026-0066
JUSTC, **2026**, 56(X):

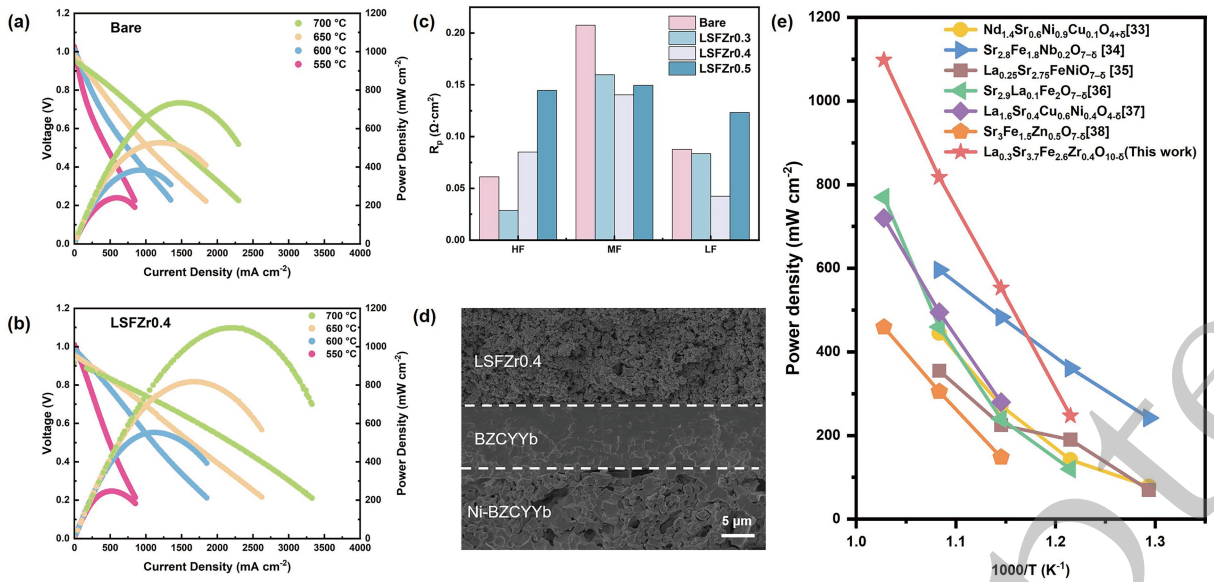

Fig. 4. LSFZr*x* single cells: (a, b) EIS Nyquist plots of Bare and *x*=0.4; (c) Fitted polarization resistances of three frequency ranges at 650 °C; (d) Cross-sectional SEM image of LSFZr0.4 single cell; (e) Comparison of PPD values with reported Co-free layered cathodes[33–38]

Bare. LSFZr0.4 exhibits the smallest polarization resistance, measuring 0.103 Ω cm^2 at 700 °C, followed by LSFZr0.5 (0.123 Ω cm^2), LSFZr0.3 (0.128 Ω cm^2), and Bare (0.148 Ω cm^2), indicating superior charge-transfer kinetics and surface exchange capability for LSFZr0.4.

These polarization resistance results are in good agreement with the I-V-P performance, confirming that an appropriate amount of Zr doping is key to optimizing the electrochemical performance of LSFZr*x* cathodes. Moreover, the lower polarization resistance of LSFZr0.4 compared with that of LSFZr0.3 confirms that an appropriate amount of Zr doping effectively optimizes the oxygen vacancy concentration and hydration capability, thereby enhancing the electrochemical activity. The smallest polarization resistance of LSFZr0.4-based cell directly supports its highest power output, providing a strong electrochemical basis for its practical application in protonic ceramic fuel cells.

To investigate the effect of Zr doping on the electrode process kinetics of LSFZr*x* cathodes, the EIS spectra of single cells were analyzed by frequency-range fitting (Fig. 4c). In the high-frequency region, the ionic transport resistance follows the order: LSFZr0.5 > Bare > LSFZr0.4 > LSFZr0.3. LSFZr0.3 shows the best ionic transport capability, which can be mainly attributed to its low Zr doping content. Such low-level Zr incorporation not only stabilizes the layered Ruddlesden–Popper structure (in comparison with SFO), but also retains a high oxygen vacancy concentration (in comparison with LSFZr0.4 and LSFZr0.5), thereby effectively promoting ionic migration kinetics.

For the mid- and low-frequency regions, the charge transfer resistance and oxygen adsorption/dissociation resistance obey the sequences of Bare > LSFZr0.3 > LSFZr0.5 > LSFZr0.4, and LSFZr0.5 > Bare > LSFZr0.3 > LSFZr0.4, respectively. LSFZr0.4 exhibits the smallest resistance values in both frequency regions, implying its remarkable catalytic activity toward charge transfer as well as oxygen adsorption and dissociation processes.

It is noteworthy that LSFZr0.4 possesses a lower oxygen vacancy concentration and inferior electronic conductivity relative to LSFZr0.3. From the perspective of defect chemistry and electronic conduction, the superior electrochemical impedance behavior of LSFZr0.4 seems counterintuitive. Such anomalous performance can be reasonably interpreted by its well-matched thermal expansion coefficient with the electrolyte. The favorable thermal expansion compatibility greatly optimizes the cathode–electrolyte interfacial contact, facilitates interfacial charge transfer, and accelerates oxygen surface exchange kinetics.

The cross-sectional SEM image of the LSFZr0.4-based single cell (Fig. 4d) reveals a dense, crack-free electrolyte layer and a well-bonded electrode/electrolyte interface. This desirable interfacial microstructure provides a solid structural foundation for the excellent electrochemical performance of the LSFZr0.4 cathode.

4 Conclusions

A series of Ruddlesden–Popper-type cathodes, $La_{0.3}Sr_{3.7}Fe_{3-x}Zr_xO_{10-\delta}$ (x = 0.3, 0.4, 0.5), have been successfully fabricated via a tailored combustion route. Electrochemical evaluations demonstrate that the LSFZr0.4 cathode exhibits the most favorable oxygen reduction reaction (ORR) performance among all as-prepared samples, featuring a minimum polarization resistance of 0.14 Ω cm^2 for the symmetric cell at 700 °C and a superior peak power density of 1098.0 mW cm^{-2} at 700 °C. This remarkable electrochemical superiority of LSFZr0.4 mainly stems from its intrinsically matched thermal expansion behavior with the electrolyte material. Such favorable thermomechanical compatibility enables intimate interfacial adhesion between the cathode and electrolyte, effectively facilitating interfacial charge transfer and oxygen surface exchange processes and thereby substantially boosting the ORR reaction kinetics. This study proves that rational Zr doping regulation is an effective route to exploit high-performance cobalt-free RP-type cathode materials, and

CSTR: 32290.14.JUSTC-2026-0066
DOI: 10.52396/JUSTC-2026-0066
JUSTC, **2026**, 56(X):

LSFZr0.4 is verified to be a promising alternative air electrode for practical PCFC applications.

Supporting information

The supporting information for this article can be found online. The supporting information includes seven figures and two tables.

Acknowledgement

This work was supported by the National Natural Science Foundation of China (52272247).

Conflict of interest

The authors declare that they have no conflict of interest.

Biographies

Xiaoxia Li obtained her master's degree from the University of Science and Technology of China. Her research mainly focuses on ammonia synthesis via protonic ceramic fuel cells.

Ranran Peng is an Associate Professor at the University of Science and Technology of China (USTC). She received her Ph.D. degree from USTC in. Her research mainly focuses on the preparation, performance, and mechanisms of solid oxide cells and related materials.

References

[1] Wang N, Tang C, Du L, et al. Advanced cathode materials for protonic ceramic fuel cells: Recent progress and future perspectives. *Advanced Energy Materials*, **2022**, *12*: 2201882.

[2] Guo Z, Xu L, Ling Y, et al. A perspective on cathode materials for proton-conducting solid oxide fuel cells. *International Journal of Hydrogen Energy*, **2025**, *106*: 52–64.

[3] Gao H, He F, Zhu F, et al. Effective promotion of the activity and stability of cathodes for protonic ceramic fuel cells. *Advanced Functional Materials*, **2024**, *34*: 2401747.

[4] He F, Zhou Y, Hu T, et al. An efficient high-entropy perovskite-type air electrode for reversible oxygen reduction and water splitting in protonic ceramic cells. *Advanced Materials*, **2023**, *35*: 2209469.

[5] Hossain S, Abdalla A M, Jamain S N B, et al. A review on proton conducting electrolytes for clean energy and intermediate temperature-solid oxide fuel cells. *Renewable and Sustainable Energy Reviews*, **2017**, *79*: 750–764.

[6] Liao Z, Yang Y, Ou D, et al. Enhanced oxygen electrode performance in solid oxide fuel cells *via* La-doping of $Pr_2NiO_{4+\delta}$-based Ruddlesden–Popper perovskites. *Journal of Materials Chemistry C*, **2024**, *12*: 19506–19514.

[7] Baharuddin N A, Muchtar A, Somalu M R. Short review on cobalt-free cathodes for solid oxide fuel cells. *International Journal of Hydrogen Energy*, **2017**, *42*: 9149–9155.

[8] Dong F, Gao Z, Zhang B, et al. Achieving exceptional activity and durability toward oxygen reduction based on a cobalt-free perovskite for solid oxide fuel cells. *Journal of Energy Chemistry*, **2021**, *62*: 653–659.

[9] Zhou L, Yin Y, Nematov D, et al. A high-performance cobalt-free cathode for proton-conducting solid oxide fuel cells *via* multi-element doping in $Sr_2Fe_2O_6$. *Sustainable Materials and Technologies*, **2026**, *48*: e01936.

[10] Xu N, Zhang S, Su S, et al. Cobalt-free perovskite $La_{0.6}Ba_{0.4}Ni_{0.2}Fe_{0.8-x}Ti_xO_{3-\delta}$(x=0–0.3) as cathode for intermediate-temperature solid oxide fuel cells. *International Journal of Hydrogen Energy*, **2024**, *50*: 1064–1074.

[11] Feng Q, et al. Synergistic modulation of oxygen vacancies and proton hydration in iron-based perovskites for protonic ceramic fuel cells. *ACS Sustainable Chemistry & Engineering*, **2026**, *14*: 3690–3698.

[12] Ye Q, Ye H, Ma Z, et al. Facile deficiency engineering in a cobalt-free perovskite air electrode to achieve enhanced performance for protonic ceramic fuel cells. *Small*, **2024**, *20*: 2307900.

[13] Ye H, Wang Y, Ye Q, et al. An advanced bifunctional single-element-incorporated ternary perovskite cathode for next-generation fuel cells. *Journal of Power Sources*, **2025**, *628*: 235875.

[14] Li X, Huan D, Shi N, et al. Defects evolution of Ca doped $La_2NiO_{4+\delta}$ and its impact on cathode performance in proton-conducting solid oxide fuel cells. *International Journal of Hydrogen Energy*, **2020**, *45*: 17736–17744.

[15] Zhu J, Gong H, Zhu J, et al. Pr_6O_{11} as an excellent oxygen catalyst enhances the electrocatalytic activity of Ruddlesden-Popper perovskite for SOFC composite cathodes. *Ceramics International*, **2026**, *52*: 9491–9501.

[16] Wang Z, Yang W, Shafi S P, et al. A high performance cathode for proton conducting solid oxide fuel cells. *Journal of Materials Chemistry A*, **2015**, *3*: 8405–8412.

[17] Kagomiya I, Jimbo K, Kakimoto K I, et al. Oxygen vacancy formation and the ion migration mechanism in layered perovskite $(Sr, La)_3Fe_2O(7-\delta)$. *Physical Chemistry Chemical Physics*, **2014**, *16*: 10875–10882.

[18] Zhang S, Dou Y, Xia T, et al. Achieving electrocatalytic activity toward oxygen reduction reaction based on Ruddlesden–Popper type cathode catalyst for solid oxide fuel cells. *Journal of Advanced Ceramics*, **2025**, *14*: 9221178.

[19] Jaiswal S, Mondal R, Kushwaha V, et al. Tuning of redox energy of transition-metal ions through the utilization of interlayer potentials in layered perovskites: Development of a titanium-based superior HER catalyst in an acidic medium. *ACS Applied Energy Materials*, **2023**, *6* (14): 7323–7334.

[20] Huan D, Zhang L, Zhu K, et al. Improving Ruddlesden-Popper electrocatalysts through interstitial fluorination-driven rearrangements of local coordination environment. *Sustainable Materials and Technologies*, **2023**, *38*: e00754.

[21] Ma T, Xia T, Li Q, et al. Boosting electrocatalytic performance of Ruddlesden-Popper type Fe-based cathode catalysts by La and Ni co-doping for solid oxide fuel cells. *International Journal of Hydrogen Energy*, **2022**, *47*: 22963–22971.

[22] Tummino M L, Liotta L F, Lo Faro M, et al. Effects of B-site doping and stoichiometry on strontium ferrate $Sr_{0.85}Ce_{0.15}Fe_xCoyO3$ perovskites as electrocatalysts. *Journal of the American Ceramic Society*, **2025**, *108*: e20528.

[23] He Y, Qiu B, Li X, et al. Microstructure-mediated effects of fuel electrode powder on the electrochemical properties of protonic ceramic cells. *International Journal of Hydrogen Energy*, **2026**, *219*: 154134.

[24] Huan Y, Zhu F, Zeng J, et al. Effect of synthesis methods on microstructure and electrochemical performance of $PrBa_{0.5}Sr0{\cdot}5Co1{\cdot}5Fe0{\cdot}5O_{5+\delta}$ cathodes for protonic ceramic fuel cells. *International Journal of Hydrogen Energy*, **2025**, *160*: 150645.

[25] Tang S, Fu M, Qin Z, et al. Topological ion optimized composite cathode for proton-conducting solid oxide fuel cells. *Advanced Functional Materials*, **2025**, *35*: 2501995.

[26] Song R, Zhang X, Huan D, et al. A novel triple-conductive cathode with high efficiency and stability for protonic ceramic fuel cells. *International Journal of Hydrogen Energy*, **2023**, *48*: 32943–32954.

[27] Rehman Z U, Zhu K, Qiu B, et al. Phase evolution and catalytic optimization of Ruddlesden-Popper cathodes for protonic ceramic fuel cells. *International Journal of Hydrogen Energy*, **2025**, *135*: 515–524.

[28] Guo G, Qiu B, Zhang L, et al. Effect of doping Fe to yttria-stabilized

CSTR: 32290.14.JUSTC-2026-0066
DOI: 10.52396/JUSTC-2026-0066
JUSTC, **2026**, 56(X):

zirconia: Sintering ability, conductivity and solubility. *International Journal of Hydrogen Energy*, **2025**, *133*: 1–11.

[29] Dong K, Hou J, Miao L, et al. A comparative study of the R-P phase Srn+1FenO3n+1 (n= 1, 2 and 3) cathodes for intermediate temperature solid oxide fuel cells. *Ceramics International*, **2020**, *46*: 19335–19342.

[30] Huan D, Shi N, Zhang L, et al. New, efficient, and reliable air electrode material for proton-conducting reversible solid oxide cells. *ACS Applied Materials & Interfaces*, **2018**, *10* (2): 1761–1770.

[31] Chung Y S, Kim T, Shin T H, et al. *In situ* preparation of a $La_{1.2}Sr_{0.8}Mn_{0.4}Fe_{0.6}O_4$ Ruddlesden–Popper phase with exsolved Fe nanoparticles as an anode for SOFCs. *Journal of Materials Chemistry A*, **2017**, *5*: 6437–6446.

[32] Tai L W, Nasrallah M M, Anderson H U, et al. Structure and electrical properties of La1 − x Sr x Co1 − y Fe y O_3. Part 2. The system La1 − x Sr x $Co_{0.2}Fe_{0.8}O_3$. *Solid State Ionics*, **1995**, *76*: 273–283.

[33] Wang W T, Wu Y T, Lin X L, et al. Highly efficient A- and B-site-doped ruddlesden–popper perovskite oxide $Nd_{2-x}Sr_xNi_{0.9}Cu_{0.1}O_{4+\delta}$ as a cathode for PCFCs. *ACS Applied Energy Materials*, **2024**, *7* (6): 2197–2209.

[34] Yu N, Bello I T, Chen X, et al. Rational design of ruddlesden–popper perovskite ferrites as air electrode for highly active and durable reversible protonic ceramic cells. *Nano-Micro Letters*, **2024**, *16*: 177.

[35] Ling Y, Guo T, Guo Y, et al. New two-layer Ruddlesden: Popper cathode materials for protonic ceramics fuel cells. *Journal of Advanced Ceramics*, **2021**, *10*: 1052–1060.

[36] Ma T, Xia T, Li Q, et al. Highly electrocatalytic activity Ruddlesden–Popper type electrode materials for solid oxide fuel cells. *Journal of the European Ceramic Society*, **2022**, *42*: 490–498.

[37] Ma J, Pan Y, Wang Y, et al. A Sr and Ni doped Ruddlesden–Popper perovskite oxide $La_{1.6}Sr_{0.4}Cu_{0.6}Ni_{0.4}O_{4+\delta}$ as a promising cathode for protonic ceramic fuel cells. *Journal of Power Sources*, **2021**, *509*: 230369.

[38] Sun Y, Liu Z, Zhou Z, et al. $Sr_3Fe_{1.5}Zn_{0.5}O_{7-\delta}$ as cathode for protonic-conducting solid oxide fuel cells with enhanced oxygen reduction reaction activity. *ECS Meeting Abstracts*, **2023**, *MA2023-01*: 158.

CSTR: 32290.14.JUSTC-2026-0066
DOI: 10.52396/JUSTC-2026-0066
JUSTC, **2026**, 56(X):